Thesis for the degree of Licentiate of Engineering

Modelling of Battery Electrolyte Interactions

Gustav Åvall

Department of Physics
Chalmers University of Technology
Gothenburg, Sweden 2018

Modelling of Battery Electrolyte Interactions

GUSTAV ÅVALL

Department of Physics
Chalmers University of Technology
SE-412 96 Gothenburg
Sweden
Telephone +46 (0)31-772 1000

This work has received funding through the EU H2020 NAIADES project (LCE10-2014, #646433) and the support from the Swedish Energy Agency through Batterifondsprogrammet: Next Generation Batteries (#37671-1).

Chalmers, Reproservice
Gothenburg, Sweden 2018

Abstract

The rechargeable lithium-ion battery (LIB), powering our portable electronics, has transformed our everyday lives. Even though the success of the LIB there is a need for next generation batteries, due to a lack of abundant lithium and a need for greater performance and sustainable chemistries, in order to move towards a sustainable society with applications such as hybrid and electrical vehicles (EVs) and large scale energy storage for solar and wind power. Therefore, there is a large interest in various next generation batteries, such as sodium-ion, Li-S, and Li-air batteries.

In this thesis the structure of Li^+ and Na^+ solvation shells, as functions of salt concentrations, is studied using a semi-empirical method. Overall, this shows that: *i)* The first solvation shell of the Na-ion is larger and more disordered than the Li-ion first solvation shell, *ii)* The coordination number (CN) remain quite constant as a function of concentration, while the disorder, as measured by the variance of the CN, increases with concentration, and *iii)* The choice of solvent influences the disorder. Moreover, the interaction of O_2 with several anions is computed, showing a correlation between the interaction energy and the O_2 solubility, with application to Li-air batteries. Finally, a novel approach employing *ab initio* molecular dynamics to study solvation shell dynamics is presented.

Keywords: Lithium-ion batteries, sodium-ion batteries, electrolytes, *ab initio* molecular dynamics, density functional theory, semi-empirical Methods.

List of Papers

This thesis is based on the following papers:

I *Solvation structure in dilute to highly concentrated electrolytes for lithium-ion and sodium-ion batteries*
E. Flores, G. Åvall, S. Jeschke, P. Johansson
Electrochimica Acta **2017**, *233*, 134-141.

II *Li Salt Anion Effect on O_2 Solubility in an Li-O_2 Battery*
J. Lindberg, B. Endrődi, G. Åvall, P. Johansson,
A. Cornell, G. Lindbergh
The Journal of Physical Chemistry C **2018**, *122*, 1913-1920.

III *Sodium-Ion Battery Electrolytes: Modeling and Simulations*
G. Åvall, J. Mindemark, D. Brandell, P. Johansson
Advanced Energy Materials **2018**, *8*, 1703036.

Contribution Report

I I performed the computations, suggested the variance as a measure of disorder, analysed the data along with co-authors, co-authored the main part of the manuscript with E. Flores.

II I performed the computational part of the study, and authored the computational part of the manuscript.

III I wrote the liquid electrolytes part of the review.

Table of Contents

Chapter 1

Introduction

Rechargeable batteries have reshaped our society. Ever since Sonys Li-ion battery (LIB) hit the market in 1991 offering 200 Wh/l, which has by now more than tripled to 650 Wh/l [1], we have seen a transformation of our everyday life with practical portable electronics, not least of which, the smartphone. Furthermore, as the world faces the effects of climate change and try to mitigate the damage, batteries emerge as a promising technology in the transition to a CO_2 neutral society. In particular, the hybrid and electrical vehicle (EV) market hinges on the availability of high performance batteries. As the transport sector contributes *ca.* 20% to the release of CO_2 into the atmosphere [2, 3], batteries are crucial for reducing emission in the transport sector. Moreover, in 2016 the World Economic Forum ranked next generation batteries as a most important emerging technology (second only to Nanosensors and the Internet of Nanothings). This is due to their proposed role as large energy storage for wind and solar energy, enabling on demand energy availability [4, 5].

The main components of an electrochemical cell, often also called a battery even if technically this also includes the current collectors, the casing of the cell, and multiple cells along with supporting electronics, are the electrodes containing the energy, and the separator containing the electrolyte and separating the electrodes to prevent short-circuiting. The role of the electrolyte is to enable efficient transport of ions between the electrodes during charge/discharge, as the electrons move in an outer circuit. The electrolyte has an important role in several possible areas of battery improvements, such as: *i)* Enabling a wider electrochemical stability window (ESW), allowing for cycling at higher voltages [6], *ii)* More effective dissolution of O_2 for Li-air batteries, increasing capacity, *iii)* Effective ion solvation and desolvation, facilitating faster charging and discharging, and *iv)* Improved cationic conductivity, increasing power density.

Computational studies enable an alternative to the often costly and time consuming work of synthesising and characterizing novel battery materials.

Modelling can also offer information on the fundamental processes underlying the operation of the battery. For instance, the standard study of the highest occupied molecular orbital (HOMO) and lowest unoccupied molecular orbital (LUMO), reveals information on the ESW.

In this thesis the semi-empirical method PM7 have been employed in order to study the structure of solvation shells. This method is based on the Hartree-Fock (HF) formalism, but some two-electron integrals are omitted or approximated, while other parameters are determined from experimental data. In order to study the dynamics of the first solvation shell *ab initio* molecular dynamics (AIMD) as implemented in Car-Parrinello molecular dynamics (CPMD) is used. Moreover, interaction energies between O_2 and anions have been calculated using density functional theory (DFT).

The structure and dynamics of the cationic solvation environment is crucial for the understanding of the electrolytes transport properties, along with charging/discharging. A semi-empirical study of the cationic first solvation shell structure as a function of salt concentration was performed for $Li/NaPF_6$ in acetonitrile (ACN), or propylene carbonate (PC), systems. The structure has implications on the liquid range and the desolvation mechanism along with transport properties. This was studied further using CPMD to gain accuracy and information on the dynamics.

Computing the interactions of different electrolyte species; solvents, and anions, with molecular O_2 has been used to garner information on oxygen solubility in electrolytes. The O_2 solubility is crucial for the operation of a Li-air battery, as the oxygen acts as the cathode and hence must be soluble in large concentration in order to reach high capacities and ultimately high energy density for the battery.

Overall, the thesis aims to use computational studies of local phenomena to enable optimization and understanding of macroscopic properties for various modern battery chemistries. Furthermore, method development is included to target desolvation/ligand-exchange phenomena and transport mechanism(s) in highly concentrated electrolytes via the distribution of forces on solvent molecules.

Chapter 2

Batteries

A battery is an electrochemical device which is able to store chemical energy and convert it into electrical energy when needed. There are four main components in a battery: *i)* The cathode, acting as the positive electrode during discharge, where reduction occurs, *ii)* The anode, the negative electrode during discharge, where oxidation occurs, *iii)* The electrolyte, which facilitates migration of ionic species between the electrodes, and *iv)* The separator, which hosts the electrolyte and hinders short-circuiting by providing a physical barrier between electrodes. The theoretical voltage, E_{cell}, is determined by the redox reactions taking place at the electrodes. For a LIB (Figure 2.1), with the today common graphite and $LiCoO_2$ (LCO) electrodes, the reactions during discharge are:

Reduction at anode:	$LiC_6 \longrightarrow C_6 + Li^+ + e^-$
Oxidation at cathode:	$Li^+ + e^- + CoO_2 \longrightarrow LiCoO_2$
Total reaction:	$LiC_6 + CoO_2 \longrightarrow C_6 + LiCoO_2$

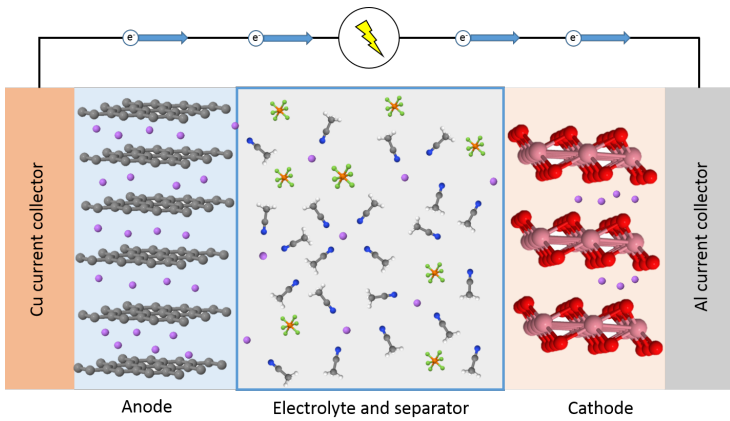

Figure 2.1: A schematic view of a LIB during discharge. Li^+ (purple) moves from the anode to the cathode, while electrons move in an external circuit.

The change in Gibbs free energy of the total reaction (ΔG) determines the theoretical voltage through Nernst equation:

$$E_{\text{cell}} = -\frac{\Delta G}{nF} \tag{2.1}$$

where n is the number of electrons participating in the reaction and F is the Faraday constant. The voltage, V, is the difference in potential between the cathode and anode

$$V = E_{cathode} - E_{anode}. \tag{2.2}$$

The voltage is limited by the theoretical voltage, but varies during discharge/charge, and hence depends on the amount of charge Q that has been transferred between the electrodes, $V = V(Q)$. How the cell voltage changes is highly dependent on the chemistry of the system, but there are in general three types of voltage profiles: *i)* Flat, the voltage is largely constant during discharge, *ii)* Multi-step, there are several plateaus in the profile and *iii)* sloping, the voltage steadily decreases during discharge [7].

The energy of a battery is stored in the electrodes, and their chemical composition determines the energy density, and in part the power density of the battery. The total energy of the cell is given by the integral

$$E = \int_0^C V(Q)dQ \tag{2.3}$$

where C is the capacity of the cell, *i.e.* the total amount of charge which can be reversibly transferred. The power, P, is determined by how fast the discharge process can proceed. If an amount of charge $\Delta Q = Q_2 - Q_1$ is transferred during a time interval T the power is

$$P = \frac{1}{T}\int_{Q_1}^{Q_2} V(Q)dQ \tag{2.4}$$

The power is limited by the speed of the charge transfer process and is thus connected with the kinetics, but also the ionic transport in the electrolyte. The gravimetric and volumetric energy/power density of the cell is given by dividing the energy/power by the mass or volume of the cell, respectively.

The electrolyte, composed of a mixture of salts and solvents, is an ionically conductive, but electronically insulating, medium through which the ionic species migrate between the electrodes. The electrolyte is in direct contact with the electrodes and it is, hence, possible that side reactions take place at the electrolyte/electrode interface. Therefore, it is important that the operating voltage of the battery is within the ESW, the lower bound defined as the HOMO of the electrolyte and the upper bound as the LUMO of the electrolyte (Figure 2.2). There are several additional requirements on the electrolyte, such as high ionic conductivity, allowing for high power density, a wide liquid range, non-toxicity and non-volatility.

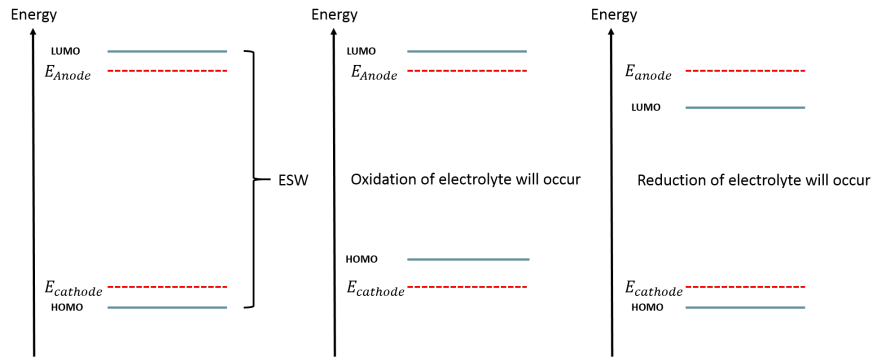

Figure 2.2: Schematic representation of the ESW. (left) The electrodes operate within the ESW and the system is stable. (Middle) The HOMO is above the operating voltage of the cathode and oxidation with the electrolyte will occur. (Right) The LUMO is below the operating voltage of the anode and reduction with the electrolyte will occur.

2.1 The Lithium-Ion Battery

LIBs display a large gravimetric energy density of ca. 200 Wh/kg, and volumetric energy density of ca. 600 Wh/l at the cell level, much greater than the energy densities of other rechargeable batteries such as NiCd and NiMH [8, 9]. Moreover, the long cycle life of LIBs make it the battery of choice for portable electronics [8] and EVs [7, 10].

In modern day LIBs the electrodes are often layered structures where the lithium occupy the space between the layers. During cycling the electrode material must allow for insertion/extraction of lithium, without causing a high degree of mechanical stress on the system. This process is referred to as intercalation. The capacity of the system is then limited by the amount of lithium the electrodes can accept into their structure.

2.1.1 Anodes

As an anode, lithium titanium oxide $Li_4Ti_5O_{12}$ displays a negligible effect on the crystal structure upon intercalation of lithium and reduces lithium at 1.5 V *vs.* $Li^{\circ}/\ Li^{+}$, within the ESW of the electrolyte. This makes for a stable system yielding long cycle life and reliability. However, the anode has a low specific capacity, this along with the high reduction potential leads to low energy density [11–13]. Instead, the anode of choice is graphite, displaying high specific capacity and operating at a voltage of 0.3 V *vs.* $Li^{\circ}/\ Li^{+}$ making for a high energy density system [14, 15]. The low reduction potential of graphite is outside the ESW of common electrolytes. However, upon decomposing, some electrolyte chemistries form a protective layer, the solid electrolyte interphase (SEI), on the anode surface. The SEI is ionically conductive, but electronically insulating, which allow for the electrochemical insertion process to continue while inhibiting further decomposition of the electrolyte [16, 17].

2.1.2 Cathodes

In general, the cathode consists of transition metal compounds. A notable example is the high energy density cathode LCO, which was used in Sonys original commercial device and still is found in portable electronics [14, 18]. However, due to low thermal stability and modest cycle life (500-1000 cycles) of LCO, $LiNiMnCoO_2$ (NMC), displaying similar energy densities, while offering enhanced cycling (1000-2000 cycles) and safety, is the cathode of choice for EVs [19]. The use of cobalt in LCO and NMC is a major drawback due

to the toxicity and hazardous mining conditions, as well as the use of child labour [20]. This has sparked a lot of interest in cobalt free cathodes, such as $LiMnO_2$ (LMO), having a spinel structure. LMO cathodes, although suffering from having a lower energy density than both LCO and NMC, has higher power density, and is made from eco-friendly materials, shows good cycle life, and thermal stability. Moreover, $LiFePO_4$ (LFP), having a olivine structure, makes for durable and eco-friendly cathodes offering long cycle life [19].

2.1.3 Electrolytes

The electrolyte of a LIB is composed of a lithium salt, a mixture of solvents, and sometimes additives. The need for a mixture of solvents and additives is due to the long list of requirements on the electrolyte. Typically, the solvents and additives are picked to serve one or several of these requirements, hoping that combining them yields an electrolyte fulfilling most requirements to a satisfactory level.

The solvents used are most often organic, mainly linear and cyclic carbonates, although aqueous electrolytes have recently attracted attention [21]. The cyclic carbonates are of interest for their high dielectric constant and their role in forming an SEI. The common cyclic carbonate being PC, having a wide liquid range and a large dielectric constant, enabling a high degree of salt dissociation [22]. However, PC only forms a stable SEI at high salt concentrations [23]. The other popular cyclic carbonate is ethylene carbonate (EC) which gained its popularity due to its ability to decompose and form a stable SEI. Moreover, EC has a high dielectric constant (89.8, higher than water), and low viscosity. But, EC has a high melting temperature of 36° C, although by using PC, or linear carbonates, as a co-solvent the electrolyte remains liquid at room temperature. Linear carbonates are mainly used for their low viscosity, yielding good ionic conductivity, and in order to enhance the liquid range. Common linear carbonates are dimethyl carbonate (DMC), diethyl carbonate (DEC), dimethoxyethane (DME), ethylmethyl carbonate (EMC) [22].

The salt needs to be able to dissolve and dissociate in the solvent in order to facilitate good ionic conductivity (>1 mS/cm). Moreover, the anion needs to be chemically inert with respect to the battery components. These requirements make weakly coordinating anions top candidates. Thus, a salt such as lithium perchlorate ($LiClO_4$) is a popular choice due to its low price, high solubility and high anodic stability. However, due to the strong oxidation nature of ClO_4^- it makes a poor anion in commercial settings. Lithium tetrafluoroborate ($LiBF_4$) shows greater safety than $LiClO_4$. How-

ever, the salt does not dissociate as easily and shows poor cyclability. Lithium bis(trifluoromethanesulfonyl)imide (LiTFSI) is proven safe, shows high thermal stability and good conductivity. But, it detrimentally corrodes the standard Al current collector which severely limits its use in commercial cells. To negate the corrosion, additives inhibiting the process has been investigated. Instead, the salt used in commercial products is lithium hexafluorophosphate ($LiPF_6$), being electrochemically stable, and although not having the best conductivity or ability to dissociate, it strikes a good balance of properties. Moreover, PF_6^- forms a passivating layer on the Al current collector, protecting the Al from corrosion [22].

Conventional LIBs have a salt concentration of *ca.* 1 M. Recently, concentrated and highly concentrated electrolytes have been under investigation. These electrolytes exhibit several advantageous properties, including non-volatility [24], and enhanced kinetics [25–27]. At these elevated concentrations the electrolyte structure is altered, becoming rich in large aggregates of ions. The unique local electrolyte structure is attributed to preventing solvent co-intercalation into graphite [25, 26, 28], and facilitates desolvation via a novel mechanism [28–30]. But, the increased salt concentration comes with an increase in cost and a lowering of the conductivity. However, a pronounce increase in alkali cation transference number has been observed, indicating an altered transport mechanism at elevated concentrations [27, 31–33].

2.2 The Sodium-Ion Battery

Moving down one period in the periodic table of elements, sodium, being more than three orders of magnitude more abundant than lithium, and an order of magnitude cheaper [34–37], makes the prospect of a sodium-ion battery (SIB) of interest. Owing to the close chemical relation of the two elements, a wealth of knowledge generated from LIB research can be applied to SIBs. Moreover, the similarities between the SIBs and LIBs makes it possible to directly use existing infrastructure in the manufacturing of SIBs [34]. The SIB promises a similar level of gravimetric energy density as LIBs [35, 38], but lower volumetric density [34], good power densities [34, 39], and is a future candidate for grid storage and E-bikes [34, 40]. Further, sodium, in contrast with lithium, does not alloy with Al, the Cu current collector in the LIB can be replaced with an Al current collector on both electrodes in SIBs, increasing the energy density and lowering cost [38, 41].

2.2.1 Anodes

Na^+ does not intercalate into a graphite anode [42, 43]. Instead, several metal oxides have been investigated as possible SIB anodes. In particular titanium oxides, the most prominent one being $Na_2Ti_3O_7$ with an insertion potential of 0.3 V, have been studied [44]. However, most of the titanium oxides have a high insertion potentials, yielding low energy densities [39]. Hard carbon, consisting of disordered stacks of graphene sheets, displaying nano-porosity, accepts Na^+ into its structure [45]. Hard carbon display a very low insertion potential, and has good capacity, making it the anode of choice in commercial cells [34].

2.2.2 Cathodes and Electrolytes

As with the LIB, the SIB cathode must be able to accommodate the Na^+, without suffering large volume expansions. Just as with LIBs, several layered oxide chemistries have been investigated [39]. In particular, cathode chemistries containing vanadium, such as $NaVPO_4F$ [46], and $Na_3V_2(PO_4)_3$ [47], have shown good cyclability and energy densities [39]. But vanadium is considered a toxic element. Instead, Prussian blue analogues and sodium nickel-oxide $NaNi_{1-x-y-z}Mn_xMg_yTi_zO_2$ are being used in commercial SIBs [34]. The electrolytes investigated and used for SIBs are in large parts the same as those for LIBs, using the sodium counter parts of the salts [48].

Chapter 3

Theory and Methods

Here a more detailed description of the microscopic structure of bulk electrolytes is presented along with the theory and methods used to study its local structure and dynamics.

3.1 A Microscopic View of Electrolytes

The LIB and SIB electrolytes most often consists of monoatomic cations and anions along with solvent species. The solvents, although neutral, have an electromagnetic multipole-moment and thus interact with the charged species. Therefore, solvent molecules in the vicinity of a cation will interact and align with the spherically symmetric electric field around it (Figure 3.1). This gives rise to a local structure; the *first solvation shell* or simply the solvation shell. Outside the first solvation shell the *second solvation shell* is found. The solvent molecules in the second solvation shell are still aligned, but to a much smaller extent due to the attenuation of the electric field from the cation. Outside the second solvation shell the effect of the cation is hardly noticeable. If the first solvation shell is a stable structure it will diffuse as one unit; vehicular transport.

At very low salt concentrations the average distance between cations and anions is great, and the above description is quite accurate especially as weakly coordinating anions are employed. However, in standard battery electrolytes the salt concentration is high enough (1 M) that stronger effects of the anion on the cation solvation shell cannot be ignored. Anions will start to become more present in the first and second solvation shell, forming contact ion pairs and solvent separated ion pairs, respectively, with the cation. At even higher concentrations the notion of a solvation shell breaks down as the ions and solvent molecules start to form aggregates (Figure 3.2). As the cations no longer exist within stable shells the transport mechanism deviate from vehicular transport and grows complex [31, 32, 49–52]. Moreover, the

content and stability of the cation solvation shells or equivalent are not only important for the transport mechanism, but play a role in the formation and structure of the SEI [53, 54].

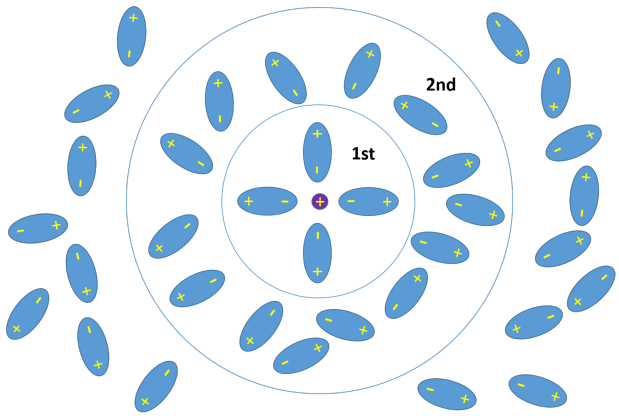

Figure 3.1: The first and second solvation shell of a cation (purple) at concentrations where the presence of an anion can be disregarded. In the first solvation shell the dipole moment of the solvents (blue) align with the radial electric field of the cation. In the second solvation shell the dipoles are still somewhat aligned with the electric field. Outside the second solvation shell the presence of the cation is hardly noticed on the structure.

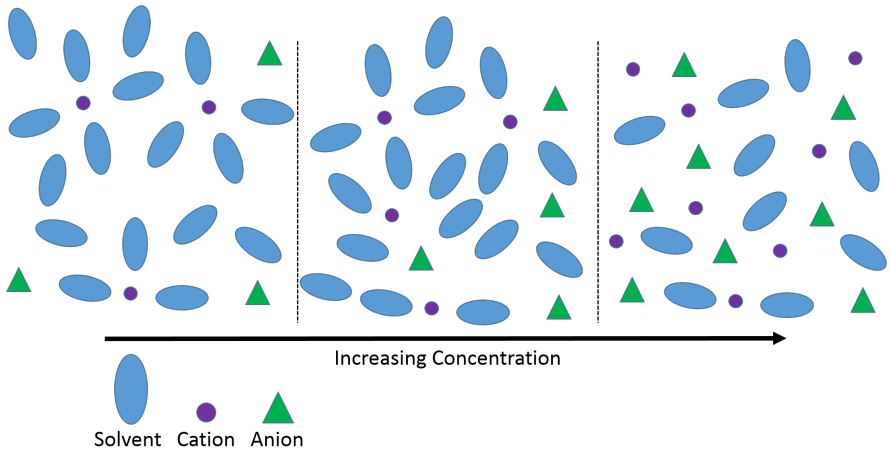

Figure 3.2: (Left) At low concentrations the first solvation shell consist of solvent molecules. (Middle) When the concentration increases anions start to make a presence in the first solvation shell. (Right) At high concentrations cation-anion aggregates form.

The content and size of the solvation shell or the equivalent at elevated concentrations can be studied by the *radial distribution function* (RDF). The RDF counts the density of atomic species around the cation

$$g_i(r) = \frac{n_i(r)}{4\pi r^2 \Delta r}, \tag{3.1}$$

where $n_i(r)$ is the number of atomic species i within a spherical shell of thickness Δr and radius r. A typical RDF (Figure 3.3) shows a clear first peak. The end of this peak, the position of the first minimum in the RDF, defines the size of the first solvation shell.

By integrating the RDF up to the first minimum, the average number of ligands, the coordination number (CN), can be calculated. Depending on the solvents and anions in the electrolyte, however, the cation may form several coordinating bonds to the same solvent molecule or anion. It is then important to distinguish the CN from the solvation number (SN) defined by the number of anions and solvent molecules in the first solvation shell.

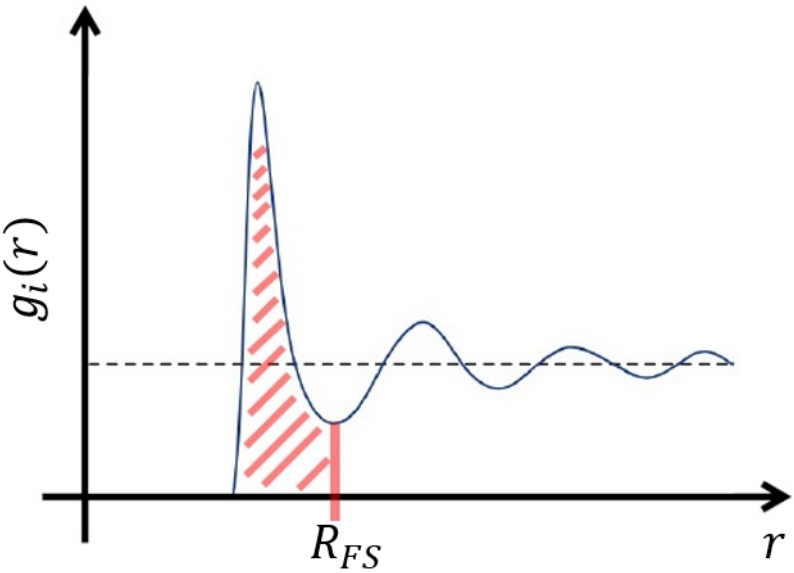

Figure 3.3: A typical RDF. The first minimum defines the size R_{FS} of the first solvation shell, and the area under the curve (red) equals the CN.

The geometry of the solvation shell can be further studied by computing the angle between the cation and coordination bonds (Figure 3.4). This reveals possible point group symmetries of the solvation shell. Furthermore, the angle between the cation and coordination bonds makes it possible to discern if the cation coordinates to multiple sites on the anions and solvent molecules.

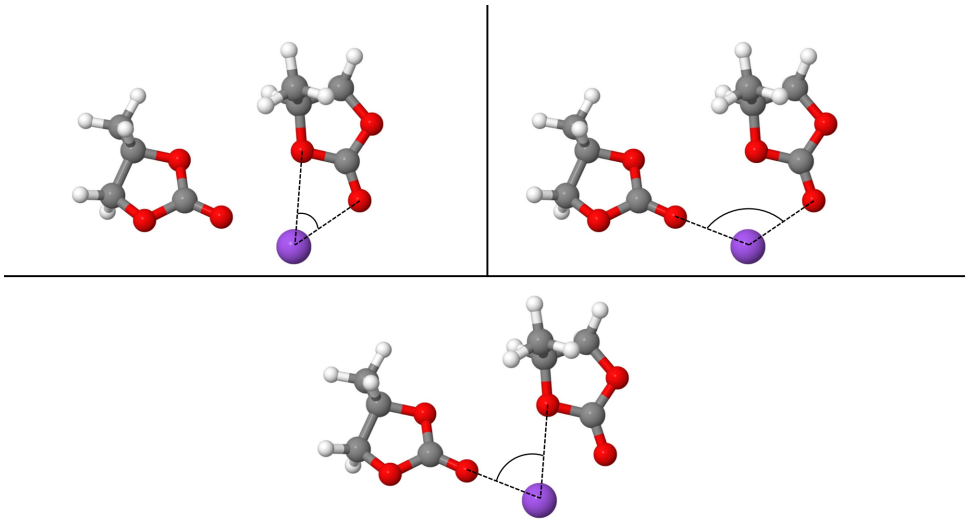

Figure 3.4: The angle between two coordinating oxygen atoms (red) and the cation (purple). The angle is smaller when the oxygen atoms belong to the same solvent molecule.

3.2 Computational Methods

To study the cation solvation shells within the electrolyte at hand the electrons and nuclei, which make up the solvent molecules and ions - both cations and anions, need to be modelled accurately - and at these length scales quantum mechanical effects become important. If N electrons of mass m_e and K nuclei with masses m_j, make up the electrolyte, the state of the system is determined by the Schrödinger equation, and in particular, the stationary states are governed by the time-independent Schrödinger equation (TISE):

$$H\Psi(\mathbf{r}_1,\ldots,\mathbf{r}_N,\mathbf{R}_1,\ldots,\mathbf{R}_K) = E\Psi(\mathbf{r}_1,\ldots,\mathbf{r}_N,\mathbf{R}_1,\ldots,\mathbf{R}_K) \tag{3.2}$$

with the Hamiltonian operator

$$\begin{aligned} H = &-\sum_{i=1}^{N}\frac{\hbar^2}{2m_e}\nabla_i^2 - \sum_{j=1}^{K}\frac{\hbar^2}{2m_j}\nabla_j^2 - \frac{1}{8\pi\varepsilon_0}\sum_{i,j}\frac{e^2 Z_j}{|\mathbf{r}_i-\mathbf{R}_j|} \\ &+ \frac{1}{8\pi\varepsilon_0}\sum_{i\neq j}\frac{e^2}{|\mathbf{r}_i-\mathbf{r}_j|} + \frac{1}{8\pi\varepsilon_0}\sum_{i\neq j}\frac{e^2 Z_i Z_j}{|\mathbf{R}_i-\mathbf{R}_j|} \end{aligned} \tag{3.3}$$

where r_i and R_j refer to electron and nuclei positions, respectively, e is the elementary charge and Z_j nuclear charges. The TISE is a non-separable partial differential equation who grows exponentially in computational complexity with the size of the system, making it monumentally difficult to solve for realistic systems [55]. To make headway the Born-Oppenheimer approximation is applied. This approximation relies on the fact that the proton is three orders of magnitude more massive than the electron and hence electronic velocities are much greater than those of nuclei. Therefore the electrons can be viewed as moving in a field generated by static nuclei and this allows for the decomposition of the wavefunction into its electronic and nuclear components

$$\Psi(\mathbf{r}_1, \ldots, \mathbf{r}_N, \mathbf{R}_1, \ldots, \mathbf{R}_K) = \psi(\mathbf{r}_1, \ldots, \mathbf{r}_N, \mathbf{R}_1, \ldots, \mathbf{R}_K)\xi(\mathbf{R}_1, \ldots, \mathbf{R}_K) \tag{3.4}$$

where $\psi(\mathbf{r}_1, \ldots, \mathbf{r}_N, \mathbf{R}_1, \ldots, \mathbf{R}_K)$ is the electronic wavefunction and $\xi(\mathbf{R}_1, \ldots, \mathbf{R}_K)$ the wavefunction of the nuclei. The electronic wavefunction is now determined using the Born-Oppenheimer Hamiltonian [56, 57]

$$H_{BO} = -\sum_{i=1}^{N} \frac{\hbar^2}{2m_e}\nabla_i^2 + \frac{1}{8\pi\varepsilon_0}\sum_{i\neq j}\frac{e^2}{|\mathbf{r}_i - \mathbf{r}_j|} - \frac{1}{8\pi\varepsilon_0}\sum_{i,j}\frac{e^2 Z_j}{|\mathbf{r}_i - \mathbf{R}_j|}. \tag{3.5}$$

In practice the electronic wavefunction itself must be represented in some fashion. This is for local and molecular systems usually done by constructing the single electron wavefunction, or *molecular orbital*, ϕ_i from a superposition of *atomic functions* χ_μ, which are functions centred on the individual atoms:

$$\phi_i = \sum_\mu C_{i\mu}\chi_\mu \tag{3.6}$$

where i enumerates the molecular orbitals, μ the atomic functions and $C_{i\mu}$ is the molecular orbital coefficients. The atomic functions are not necessarily orthogonal and are in turn represented as a linear combination of more basic functions, called *primitives*, such as Gaussian functions or Slater-type orbitals [57].

3.2.1 Hartree-Fock Theory

One approach of computing the electronic wavefunction under the Born-Oppenheimer approximation is by a procedure due to Hartree and Fock. The HF method relies on the following two assumptions: *i)* The total electronic wavefunction can be written as a single Slater determinant and, *ii)* Electrons only interact

with one-another through a mean field [56, 57]. These assumptions yields the Roothaan-Hall (RH) equation

$$\mathbf{FC} = \boldsymbol{\varepsilon}\mathbf{SC} \tag{3.7}$$

where:

- $\mathbf{C}$ is the matrix of molecular orbital coefficients of equation 3.6.
- $\mathbf{S}$ is the overlap matrix, and reads in component form $S_{\mu\nu} = \int \chi_\mu \chi_\nu dV$
- $\mathbf{F}$ is the Fock matrix, containing the kinetic operator, the nuclear-electron attraction operator along with the Coulomb operator
  $J\phi_i(\mathbf{r}) = \phi_i(\mathbf{r}) \int \frac{|\phi_j(\mathbf{r}')|^2}{|\mathbf{r}' - \mathbf{r}|} d\mathbf{r}'$ and the exchange operator
  $K\phi_i(\mathbf{r}) = \phi_j(\mathbf{r}) \int \frac{\phi_j(\mathbf{r}')^* \phi_i(\mathbf{r}')}{|\mathbf{r}' - \mathbf{r}|} d\mathbf{r}'$.

The RH equation depends on the orbitals through the Coulomb and exchange operator in the Fock matrix and is hence solved self-consistently [56, 57].

3.2.2 Semi-Empirical Methods

Semi-empirical methods are a group of methods which rely on empirical data or data from higher level methods to drastically cut the computational cost of solving the RH equation. One family of semi-empirical methods are those based on the neglect of diatomic differential overlap (NDDO), meaning that the overlap matrix $\mathbf{S}$ is reduced to a unit matrix. A subset of the NDDO methods are the parametrized methods (PM). All PM methods use parameters, which have been optimized using empirical data in order to yield accurate energies, to partially determine off-diagonal elements in the Fock matrix [58, 59]. In this thesis PM7 is used, which solved some known issues with the NDDO algorithm and used a larger set of empirical and *ab initio* data, compared with its predecessors, in their parametrization procedure. Overall, this reduced the unsigned error on several important properties compared with PM6, in particular the unsigned error on bond distances were reduced by 10%. In addition, it should be noted that PM6 and PM7 are designed to increase accuracy on simulation of biochemical macromolecules [58].

3.2.3 Density Functional Theory

In practice, the majority of electronic structure calculations are today done using DFT [56]. DFT is based on the discovery of Hohenberg and Kohn that there is a unique map between the ground state properties of a many-electron system and the electron density

$$n(\mathbf{r}) = \sum_{i=1}^{N} |\psi_i(\mathbf{r})|^2 \tag{3.8}$$

where $\psi_i(\mathbf{r})$ are single-electron wavefunctions. The electron density is a function of only the three spatial dimensions and thus the number of variables are drastically reduced [60]. Therefore, the ground state energy of the system can be determined from the electron density and is given by

$$\begin{aligned} E_0 =& T[n(\mathbf{r})] + \int_{R^3} V_{nuclei}(\mathbf{r}) n(\mathbf{r}) d\mathbf{r} \\ &+ \frac{1}{8\pi\varepsilon_0} \int_{R^3} \frac{n(\mathbf{r}) n(\mathbf{r}')}{|\mathbf{r}' - \mathbf{r}|} d\mathbf{r} d\mathbf{r}' + E_{xc}[n(\mathbf{r})] \end{aligned} \tag{3.9}$$

where $T[n(\mathbf{r})]$ is the kinetic energy functional of the non-interacting electron gas, $V_{nuclei}(\mathbf{r})$ is the potential generated by the nuclei, and $E_{xc}[n(\mathbf{r})]$ is a functional which captures the remaining energy.

In order to make use of Hohenberg and Kohns discovery the electron density must be determined. This is made possible with the Kohn-Sham equation

$$\left(-\frac{\hbar^2}{2m_e} \nabla^2 + V_{eff}(\mathbf{r}) \right) \psi_i(\mathbf{r}) = \varepsilon_i \psi_i(\mathbf{r}) \tag{3.10}$$

where

$$V_{eff}(\mathbf{r}) = V_{nuclei}(\mathbf{r}) + \frac{1}{8\pi\varepsilon_0} \int_{R^3} \frac{n(\mathbf{r}')}{|\mathbf{r}' - \mathbf{r}|} d\mathbf{r}' + \frac{\delta E_{xc}[n(\mathbf{r})]}{\delta n(\mathbf{r})}. \tag{3.11}$$

Given an initial guess of the electron density the effective potential $V_{eff}(\mathbf{r})$ can be calculated and the Kohn-Sham equation can be solved for the wavefunctions $\psi_i(\mathbf{r})$, along with an updated electron density. Using the updated electron density the procedure is repeated until self-consistency is reached [61].

The last term of equation (3.11) is called the exchange-correlation potential

$$V_{xc}[n(\mathbf{r})] = \frac{\delta E_{xc}[n(\mathbf{r})]}{\delta n(\mathbf{r})}. \tag{3.12}$$

The exchange-correlation potential is in general expanded in terms of the electron density

$$V_{xc}[n(\mathbf{r})] = V_{xc}[n(\mathbf{r}), \nabla n(\mathbf{r}), \nabla^2 n(\mathbf{r}), \dots] \tag{3.13}$$

and is subsequently approximated by one of the various functionals of DFT. The functionals are organized in a ladder, from simple and computationally cheap to accurate and computationally expensive [62]. The most basic of these functionals rely on the *local density approximation* (LDA) were the exchange-correlation functional depends only on the electron density at the selected point and thus disregards non-local effects. These functional are accurate for systems with a mostly flat electron density, *i.e.*, $\nabla n(\mathbf{r})$ is negligible. On the next level of the ladder the functionals utilizing the *generalized gradient approximations* (GGA) reside. These include a dependence on the gradient of the electron density. On the third level the kinetic energy density of the electrons are accounted for. On the fourth level, the hybrid functionals are found. Among these are the popular B3LYP functional, along with the M06 functionals employed in this thesis. The functionals on this level make use of the exact HF exchange [62].

In order to compute the equilibrium structure of a molecule, or a system of molecules, the geometry of the system is optimized. Geometry optimization utilises the gradient, with respect to nuclear coordinates, of the total energy in order to locate a stationary point in the potential energy surface (PES). As the gradient of the energy is zero at a stationary point, no force act on the system and it is in equilibrium. However, a stationary point can either be a minimum or a saddle point in the PES, corresponding to a stable equilibrium structure or a transition state, respectively. In order to ascertain the nature of the stationary point a frequency calculation can be performed. In a frequency calculation the Hessian of the energy, with respect to nuclear coordinates, is computed. The eigenvalues of the Hessian correspond to frequencies of the vibrational modes of the system. If any of these eigenvalues are negative the stationary point is a transition state [63, 64]. If all eigenvalues are positive the stationary point is a minimum. It should, however, be emphasised that there is no way to know if the structure corresponds to a local minimum or the global minimum in the PES.

As a final note on geometry optimization, all these calculations are performed at a temperature of 0 K. However, thermochemical data can still be acquired by performing a frequency calculation. With knowledge of the normal modes of the system, along with the electronic energy and the systems moment of inertia, the partition function can be calculated. From the partition function all thermodynamic properties can be computed. The accuracy

of these computations rely on how closely the system resembles an ideal gas. Moreover, the first excited electronic state is assumed to be much larger than the thermal energy k_BT [65].

3.2.4 *ab initio* Molecular Dynamics

Molecular dynamics (MD) relies on Newtons second law

$$\ddot{\mathbf{r}} = \frac{\mathbf{F}}{m} \tag{3.14}$$

to calculate the dynamics of particles. In each step of an MD simulation the forces on each particle is calculated. A time step is then taken, updating the positions of all particles. With these new positions a new set of forces are calculated and the procedure is repeated.

MD methods differ in how the forces are calculated. In particular, AIMD employs quantum mechanical *ab initio* methods in order to compute the forces. However, in practice what is referred to as AIMD often uses DFT (which is traditionally not considered an *ab initio* method within the quantum chemistry community) in order to evaluate the electron density and compute the forces on the nuclei. Updating the electron density at each time step is, however, computationally expensive [56], which is tackled by the method of Car and Parrinello by combining the quantum mechanical approach with classical approaches to MD [66]. As the total energy is the electronic energy plus the electrostatic energy of the nuclei, the total energy can be written as a functional of the electronic wavefunctions and the nuclear positions,

$$E_{tot} = E_{tot}[\{\psi_i\}, \{\mathbf{R}_j\}]. \tag{3.15}$$

Furthermore , Car and Parrinello used that the electronic wavefunctions fulfil the orthonormality condition $\langle\psi_i|\psi_j\rangle = \delta_{ij}$. The total energy can then be computed with the variational principle by minimizing $E_{tot}[\{\psi_i\}, \{\mathbf{R}_j\}]$ and the electronic structure not computed exactly for each nuclear position, *i.e.*, not in every time step of the MD simulation, as the nuclear positions are varied simultaneously with the electronic orbitals [56]. Moreover, to endow the electrons with kinetic energy a fictitious time dependence is assigned to the electronic wavefunctions which allowed for the construction of a classical Lagrangian

$$L(\{\psi_i\}, \{\mathbf{R}_j\}) = \frac{\mu}{2}\sum_{i=1}^{N}|\dot{\psi}_i|^2 + \frac{1}{2}\sum_{j=1}^{K} M_j\dot{\mathbf{R}}^2 + E_{tot}(\{\psi_i, \mathbf{R}_j\}) + \sum_{kl}\Lambda_{kl}\langle\psi_l|\psi_k\rangle. \tag{3.16}$$

Here the parameter μ in the electronic kinetic energy term is a fictitious electron mass. The mass must be chosen small enough so the electronic wavefunctions can adapt to the changing position of the nuclei but large enough to allow for large time steps. Furthermore, Lagrange multipliers Λ_{kl} are introduced in order to fulfil any external constraints, such as the orthonormality condition, at each time step. The Euler-Lagrange equation of motions are

$$\begin{cases} \mu\ddot{\psi}_i = -\dfrac{\partial E_{tot}}{\partial \psi_i} + 2\sum_j \Lambda_{ij}\psi_j \\ M_j\ddot{\mathbf{R}}_j = -\dfrac{\partial E_{tot}}{\partial \mathbf{R}_j} + \sum_{kl} \Lambda_{kl} \dfrac{\partial \langle \psi_k | \psi_l \rangle}{\partial \mathbf{R}_j} \end{cases} \tag{3.17}$$

which are solved in CPMD [56].

3.3 Ligand-Exchange Rate and Force Distributions

As previously described, at normal battery electrolyte concentrations the anions have an active role in the solvation shell. At even higher concentrations the solvation shell becomes unstable, larger aggregates form, and the content of the "first solvation shell" is continuously exchanged. This can occur through two main processes:

- Associative process: An additonal solvent molecule or anion enters the solvation shell of the cation, temporarily increaseing the cations SN by one. One of the original solvent molecules or anions in the solvation shell then exits the solvation shell, bringing the SN down to its original value.

- Dissociative process: A solvent molecule or anion exits the solvation shell of the cation, temporarily decreasing the cations SN by one. Another solvent molecules or anions in close proximity to the solvation shell then enters it, raising the SN up to its original value.

Both of these process represent an exchange of ligands, and the rate of these processes is given by the ligand-exchange rate.

It is very difficult to accurately model the ligand-exchange rate due to the complex structure of the electrolyte. Ligand-exchange rates have, however, been studied by running large classical MD simulations in order to gather data on how often a ligand-exchange occurs [51], but the accuracy depends on the force field and yields no information on what governs the underlying process of ligand-exchange.

In order for an exchange of ligands to occur, in both the associative and dissociative process, a solvent molecule or anion has to exit the first solvation shell, meaning the centre of mass of the solvent molecule or anion has to move beyond some critical distance from the cation. Thus the system can be simplified by only consider the position of the centre of mass of solvent molecules and anions (Figure 3.5).

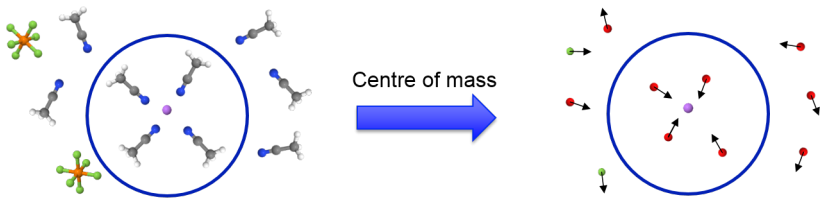

Figure 3.5: The content of the first solvation shell is defined as all molecules and anions within a critical distance (blue circle) of the cation (purple). The solvents and anions are replaced by fictitious particles at the anions (green) or solvents centre of mass (red) and the total force (arrows) are studied.

Therefore, the centre of mass dynamics along the radial direction from the cation is crucial for the understanding of ligand-exchange. Moreover, the radial motion of the centre of mass is completely determined by the radial component of the total force acting on the solvent molecule or anion through Newton's second law. For a solvent molecule or anion with centre of mass position r, then

$$m\ddot{r} = F_{tot}(r, \dot{r}, t) = F(r) - \eta\dot{r} + \tilde{F}(r, t) \tag{3.18}$$

Here, m is the mass of the species under consideration, $F(r)$ is a force term due to the interaction between the cation and the species multipole moment, the second term describes viscous forces, and, finally, $\tilde{F}(r, t)$ is a stochastic force. Just like in Brownian motion, the stochastic part of the total force comes about due to the ever fluctuating environment of the solvation shell.

It is now possible to reformulate the question of ligand-exchange rate in mathematical terms: Given a particle of mass m at initial position r_0 under the influence of a stochastic total force $F_{tot}(r, \dot{r}, t)$. What is the average time for the system to evolve such that the particle position $r > r_c$, where r_c is some critical distance greater than r_0?

The difficulty of this question hinges on the exact form of the force distribution. However, this force distribution should be highly dependent on the composition of the electrolyte and thus the force distribution becomes a possible route to directly investigate how the electrolyte composition affects ligand exchange. Moreover, the sign of the force on solvents and anions in the region between shells should reveal if the associative or dissociative process dominate. In this thesis a qualitative analysis of the force distribution on solvent molecules in an electrolyte of $LiPF_6$ in ACN was performed.

Chapter 4

Results and Discussion

Here the results of the appended papers dealing with employing PM7 and DFT simulations to reveal: *i)* O_2-anion interactions, along with how the interaction energy is affected by replacing Li^+ with Na^+ (4.1), *ii)* The solvation shell structure of Li^+ and Na^+, and how the solvation shell structure changes with concentration (4.2), as well as preliminary results on the force distribution on electrolyte solvent molecules (4.3), are summarized.

4.1 Interaction Energies

The electronic interaction energy ΔE of a complex containing N species is the energy needed to completely separate the species from one another. Thus, it is computed by taking the difference in energy of a complex containing all the species, and the energy of the separate species:

$$\Delta E = E_{complex} - \sum_{i=1}^{N} E_i \tag{4.1}$$

where $E_{complex}$ is the energy of the complex and E_i the energy of species i. If the complex consist of an ion-pair the interaction energy is commonly referred to as the ion-pair dissociation energy, as it is the energy required to dissociate the ions. If the complex consist of a cation and solvent, this energy is referred to as the solvation, or desolvation energy - much depending on the purpose and perspective.

In practice, this entails geometry optimization of the complex and the species separately. There are some nuances in this procedure, as in some studies there is no optimization of the species, in order to exclude the relaxation energy from the complex geometry to the "free" geometry [67][68]. However, in this thesis and in most studies, all structures, both complexes and "free" species are all optimized.

4.1.1 O_2-Anion Interactions

In paper II, the interaction energy was used to study the effect of different lithium salts on the O_2 dissolution capacity of dimethyl sulfoxide (DMSO) based electrolytes. Experimentally a clear correlation of O_2 solubility as a function of salt concentration (0.05, 0.5 and 1.0 M) was obtained. However, this trend was either positive or negative, depending on the anion being used, indicating that the anion is directly involved in solvating O_2. The effect on the solubility of three common salts LiTFSI, lithium triflate (LiTf) and $LiClO_4$ was investigated. Structures of [O_2:DMSO], $[O_2{:}ClO_4]^-$, $[O_2{:}Tf]^-$, and $[O_2{:}TFSI]^-$ complexes were optimized and the electronic energies computed using DFT in Gaussian 09 at the M06-2X/6-31+G(d,p) level applying the PCM implicit (continuum) solvent model using DMSO parameters to mimic the condensed phase [69, 70]. A sampling over several starting geometries was made for each type of complex, discarding all but the energetically most stable structures. Frequency calculations on the optimized structures were made in order to also discard transition states, and in the end 2 [O_2:DMSO], 2 $[O_2{:}ClO_4]^-$, 3 $[O_2{:}Tf]^-$ and 2 $[O_2{:}TFSI]^-$ stable complexes corresponding to local energy minima structures were found.

We found the solubility of O_2 to increase upon increasing the concentration of TFSI, while the O_2 solubility remained constant, or decreased, when using Tf and ClO_4^-, respectively (Figure 4.1). This indicates that TFSI promotes O_2 solubility and indeed the interaction energy between TFSI and O_2 is more than twice that of DMSO and O_2 (for the most stable structures), while for Tf it is comparable - and experimentally the solubility is constant. Finally, the interaction energy between O_2 and ClO_4^- is weaker and the solubility also decreases with $LiClO_4$ concentration.

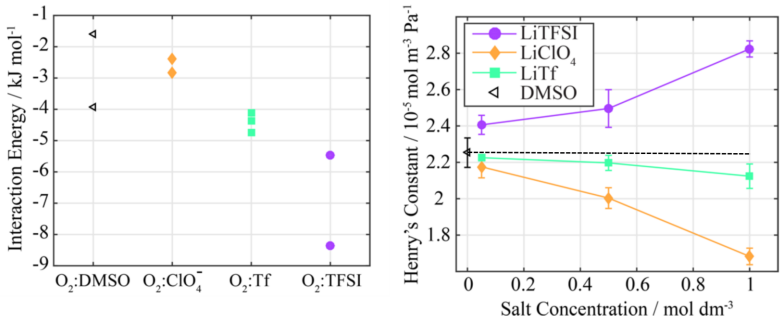

Figure 4.1: (Left) Interaction energies of O_2 with DMSO, ClO_4^-, Tf and TFSI. O_2 interacts strongest with TFSI. (Right) O_2 solubility as a function of salt concentration. Increasing the amount of TFSI increases the O_2 solubility. Reprinted with permission from *The Journal of Physical Chemistry C* **2018**, *122*, 1913-1920. Copyright 2018 American Chemical Society.

4.1.2 Interactions with Li^+ *vs.* Na^+ Cations

Several computational studies have investigated the ion-ion and ion-solvent interaction energies of electrolytes for both LIBs and SIBs [67, 68, 71–73]. Quite generally, regardless of the exact ion-ion or ion-solvent interactions being investigated, the interaction energies are lowered by *ca.* 20% upon using Na^+ instead of Li^+ as the cation.

To further investigate the difference in the interaction energies of Li^+ and Na^+ the interaction energy is decomposed into electrostatic, polarization, exchange, repulsion and dispersion contributions. The decomposition reveals that the majority of the contributions to the interactions are electrostatic, a substantial part is due to polarization, but these differ between the cations; more electrostatic for Na^+ than for Li^+, while more due to polarization for Li^+. This is due to the smaller ionic radius of Li^+ than Na^+, hence the outer electrons of Li^+ are in closer proximity to the coordinating anions and solvents, making them more susceptible to polarization effects [67, 68] - upon anion coordination the energy of the Li^+ $1s^2$ orbital is more affected than the energy of the Na^+ $2s^2$ orbital [72].

4.2 First Solvation Shell Structures for Li^+ *vs.* Na^+ Cations

In paper I the cation first solvation shell structures, for electrolytes of $Li/NaPF_6$ in ACN or PC, were investigated as functions of salt concentration. PM7 geometry optimizations of large complexes (up to 272 atoms, excluding hydrogen) were carried out, with Andreas Klamt's COSMO solvation model [74], and the CN within a distance corresponding to the first minimum in the RDF showed no clear correlation between the CN and the concentration. The observed concentration independence of the CN was not investigated further, however, it is consistent with several studies [31, 32, 52, 75, 76]. The obtained CN of Li^+ was *ca.* 4.7 and as the general consensus is that the CN of Li^+ is *ca.* 4 [22, 77–79], our approach seems to overestimate the CN somewhat. There are several possible causes for this discrepancy, including how the system environment was modelled, the temperature being 0 K, or the importance of polarization effects when studying Li^+. Also the experimental measures used to arrive at the consensus are time- and method-dependent. Correspondingly, the Na^+ CN was *ca.* 6, in line with previous studies [79–81]. The higher CN of Na^+ compared to Li^+ is due to the difference in ion radius, increasing the distance between coordinating anions and solvent molecules for Na^+, compared to Li^+, making for a larger shell. Furthermore, due to the higher CN of Na^+ compared to Li^+ the concentration at which no free solvent molecules are present will occur at lower solvent to salt ratios and hence an electrolyte employing Na^+, rather than Li^+, will display highly concentrated behaviour at lower salt concentrations.

By studying the variance of the distribution of CNs, the disorder of the first solvation shell was quantified. The first solvation shell is well-defined and solvent rich for "normal" $\sim$ 1 M concentrations, while disordered and rich in anions for higher salt concentrations (3-5 M). The trend of increased disorder was more pronounced for Na^+ than Li^+, in line with Na^+ showing highly concentrated behaviour at lower concentrations than Li^+, and more so for PC than ACN. By examining the angle between the cation and coordination sites, measured as the O-cation-O and N-cation-N angles, respectively, the difference between the PC and ACN based electrolytes was found to be due to a propensity for bidentate PC coordination for the higher salt concentrations.

The high CN variances were interpreted as a multitude of stable solvation structures, reflecting a flexible character of the solvation shell. Moreover, as these electrolytes are solvent deficient, the cations are forced to compete for the content of their solvation shells. Hence, the solvation shells formed at high

concentrations are not energetically stable compared to those obtained at lower salt concentrations. Therefore, desolvation should/could occur more easily, facilitating faster charge transfer kinetics. This also indicates that higher salt concentrations, higher variance of the CN, and more unstable solvation structures might lower the residence time of any ligand in the first solvation shell making possibilities also for the cation to move out of the shell. Therefore, vehicular transport is not necessarily the mechanism by which the cations are transported, as indeed observed in several studies [27, 31–33, 82]. Furthermore, increasing the salt concentration and the resulting higher degree of disorder should make it harder to crystallize the electrolytes and thus extend their liquid ranges - a most wanted feature practically, *i.e.*, low temperature operating batteries.

4.3 Force Distributions for Electrolyte Solvents

As a first step of studying ligand-exchange rates (see 4.2) and desolvation (see 4.1) by the method outlined in section 3.3 the force distributions on the electrolyte solvents in the first and second cation solvation shells are computed (Figure 4.2). CPMD was employed to a system consisting of $LiPF_6$ in ACN and for three salt concentrations (solvent to salt ratios): 20:1, 10:1, and 5:1. After the systems were equilibrated for *ca.* 1-2 ps, production runs of a few ps were performed. The trajectories of the production runs were subsequently analysed in order to retrieve the radial force distributions on the solvents, which broadened with increasing salt concentration (lower ratio). Furthermore, the area between the first and second solvation shell becomes more populated as the salt concentration increases, indicating either more structural disorder or an increasing ligand-exchange, *i.e.* dynamic disorder, or both. Finally, the distance between the first and second solvation shell shortens as the salt concentration increases, and hence the interactions between the shells increase, which we tentatively interpret also as a destabilized first solvation shells.

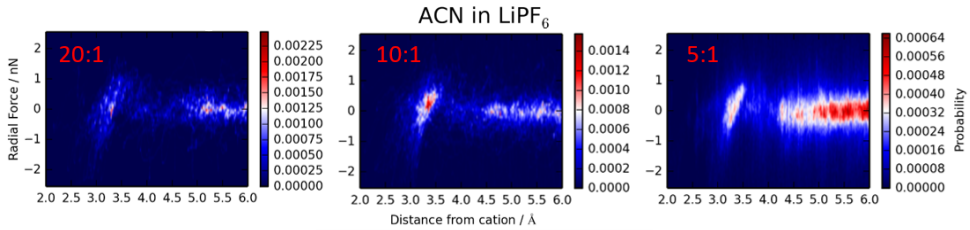

Figure 4.2: The colors indicate probability of having a certain radial force at a certain distance from a cation, with red indicating high probability and dark blue low probability. (Left) At low concentrations the distribution is very sharp within the first solvation shell. (Middle) Increasing the concentration broadens the distribution. (Right) The broadening continues upon increasing the concentration further.

Chapter 5

Conclusions and Outlook

Na^+ displays a larger solvation shell than Li^+, promoting highly concentrated behaviour at lower solvent to salt ratios than Li^+. The structure of the first solvation shell grows disordered with increasing concentration, showing that the first solvation shell grows unstable, with implications for the transport mechanism of the electrolyte, along with promoting a larger liquid range and faster kinetics. Furthermore, the correlation is more pronounced for Na^+ than Li^+, and more so for PC than ACN, again indicating that highly concentrated behaviour is seen at lower solvent to salt ratios for Na^+ than Li^+ based electrolytes.

The solubility of O_2 in a DMSO based electrolyte was dependent on the salt concentration, and the anion used. The interaction energy between O_2 and ClO_4^-, Tf and TFSI, agreed with the experimentally observed solubility trends, showing that TFSI promotes O_2 solubility. This is of interest for Li-air batteries where the O_2 solubility determines the capacity.

The distribution of radial forces on solvent molecules further indicates that the solvation shell grows disordered with increasing concentration. The distributions further indicates that the ligand exchange rate increases with concentrations. In the future, a direct way of computing the ligand-exchange rate from the force distributions will be investigated. Moreover, using AIMD data a comprehensive structure analysis of the first and second solvation shell, in LIB and SIB electrolytes, will be carried out, with an emphasis on how the structures interact with one another.

Chapter 6

Acknowledgments

First of all I would like to thank my funders: The Swedish Energy Agency and EU H2020 NAIADES.

I thank my supervisor Patrik Johansson for giving me the freedom and resources to pursue my ideas as well as giving me the opportunity to work on several interesting projects.

To all past and present members of KMF, thank you for creating a good work environment! In particular I like to thank Steffen Jeschke, Rasmus Andersson, Piotr Jankowski, Rafael Barros Neves de Araújo, Johan Scheers, and Fabian Årén for fruitful discussions on modelling. I like to thank Matthew Sadd, Muhammad Abdelhamid, Yajing "Jenny" Yan, Simon Lindberg and Adriana Navarro Súarez for trying to teach me how batteries work, in addition to some electrochemistry. I want to thank Joakim Zaar for making the office extra fun the last 6 months. Huge thank you to my office mate Simon Lindberg for (almost) always being cheerful, for all the fun and necessary chats, and for putting up with me!

Finally, I want to thank my family and friends, whom I never see nearly enough. Thank you for all the support and for always being there!

References

(1) Li, M.; Lu, J.; Chen, Z.; Amine, K. *Advanced Materials* **2018**, *1800561*, 1800561.

(2) Davis, S. J.; Caldeira, K.; Matthews, H. D. *Science* **2010**, *329*, 1330–1333.

(3) International Energy Agency, *CO2 Emissions from Fuel Combustion 2017*; OECD: 2017; Vol. 1, pp 1–162.

(4) Cann, O. These are the top 10 emerging technologies of 2016., `https://www.weforum.org/agenda/2016/06/top-10-emerging-technologies-2016/`.

(5) Carbeck, J. These next-generation batteries could end energy poverty., `https://www.weforum.org/agenda/2016/06/next-generation-batteries`.

(6) Tan, S.; Ji, Y. J.; Zhang, Z. R.; Yang, Y. *ChemPhysChem* **2014**, *15*, 1956–1969.

(7) Berg, H., *Batteries for Electric Vehicles - Materials and Electrochemistry*; Cambridge University Press: 2015.

(8) Tarascon, J.-M.; Armand, M. *Nature* **2001**, *414*, 359–367.

(9) Reddy, T. B., *Linden's handbook of batteries*; McGraw-Hill: 2011.

(10) B. Schott A. Püttner, M. M. In *Advances in Battery Technology for Electrical Vehicles*; Woodhead Publisher: 2015.

(11) Ohzuku, T.; Ueda, A.; Yamamoto, N. *Journal of The Electrochemical Society* **1995**, *142*, 1431–1435.

(12) Ferg, E.; Gummow, R. J.; Kock, A.; Thackeray, M. M. *Journal of The Electrochemical Society* **1994**, *141*, L147.

(13) Colbow, K.; Dahn, J.; Haering, R. *Journal of Power Sources* **1989**, *26*, 397–402.

(14) Ozawa, K. *Solid State Ionics* **1994**, *69*, 212–221.

(15) Sawai, K.; Iwakoshi, Y.; Ohzuku, T. *Solid State Ionics* **1994**, *69*, 273–283.

(16) Peled, E.; Menkin, S. *Journal of The Electrochemical Society* **2017**, *164*, A1703–A1719.

(17) Peled, E. *Journal of The Electrochemical Society* **1979**, *126*, 2047.

(18) Verma, P.; Maire, P.; Novák, P. *Electrochimica Acta* **2010**, *55*, 6332–6341.

(19) Zubi, G.; Dufo-López, R.; Carvalho, M.; Pasaoglu, G. *Renewable and Sustainable Energy Reviews* **2018**, *89*, 292–308.

(20) Frankel, T. C. The Cobalt Pipeline., `https://www.washingtonpost.com/graphics/business/batteries/congo-cobalt-mining-for-lithium-ion-battery/??noredirect=on`.

(21) Suo, L.; Borodin, O.; Gao, T.; Olguin, M.; Ho, J.; Fan, X.; Luo, C.; Wang, C.; Xu, K. *Science* **2015**, *350*, 938–943.

(22) Xu, K. *Chemical Reviews* **2004**, *104*, 4303–4418.

(23) Jeong, S. K.; Inaba, M.; Iriyama, Y.; Abe, T.; Ogumi, Z. *Journal of Power Sources* **2008**, *175*, 540–546.

(24) Yamada, Y.; Yamada, A. *Journal of the Electrochemical Society* **2015**, *162*, A2406–A2423.

(25) Yamada, Y.; Furukawa, K.; Sodeyama, K.; Kikuchi, K.; Yaegashi, M.; Tateyama, Y.; Yamada, A. *Journal of the American Chemical Society* **2014**, *136*, 5039–5046.

(26) Yamada, Y.; Usui, K.; Chiang, C. H.; Kikuchi, K.; Furukawa, K.; Yamada, A. *ACS Applied Materials & Interfaces* **2014**, *6*, 10892–10899.

(27) Suo, L.; Hu, Y.-S.; Li, H.; Armand, M.; Chen, L. *Nature Communications* **2013**, *4*, 1481.

(28) Yamada, Y.; Yaegashi, M.; Abe, T.; Yamada, A. *Chem. Commun.* **2013**, *49*, 11194–11196.

(29) Abe, T.; Fukuda, H.; Iriyama, Y.; Ogumi, Z. *Journal of The Electrochemical Society* **2004**, *151*, A1120–A1123.

(30) Xu, K.; von Wald Cresce, A. *Journal of Materials Research* **2012**, *27*, 2327–2341.

(31) Forsyth, M.; Yoon, H.; Chen, F.; Zhu, H.; MacFarlane, D. R.; Armand, M.; Howlett, P. C. *The Journal of Physical Chemistry C* **2016**, *120*, 4276–4286.

(32) Chen, F.; Forsyth, M. *Phys. Chem. Chem. Phys.* **2016**, *18*, 19336–19344.

(33) Matsumoto, K.; Okamoto, Y.; Nohira, T.; Hagiwara, R. *The Journal of Physical Chemistry C* **2015**, *119*, 7648–7655.

(34) Bauer, A.; Song, J.; Vail, S.; Pan, W.; Barker, J.; Lu, Y. *Advanced Energy Materials* **2018**, *8*, 1–13.

(35) Larcher, D.; Tarascon, J.-M. *Nature Chemistry* **2015**, *7*, 19–29.

(36) Jaskula, B. W. 2014 Minerals Yearbook., `http://minerals.usgs.gov/minerals/pubs/commodity/lithium/myb1-2014-lithi.pdf`.

(37) Bolen, B. W. P. 2015 Minerals Yearbook., `http://minerals.usgs.gov/minerals/pubs/commodity/soda_ash/myb1-2015-sodaa.pdf`.

(38) Ponrouch, A.; Dedryvère, R.; Monti, D.; Demet, A. E.; Ateba Mba, J. M.; Croguennec, L.; Masquelier, C.; Johansson, P.; Palacín, M. R. *Energy & Environmental Science* **2013**, *6*, 2361–2369.

(39) Slater, M. D.; Kim, D.; Lee, E.; Johnson, C. S. *Advanced Functional Materials* **2013**, *23*, 947–958.

(40) Pan, H.; Hu, Y.-S.; Chen, L. *Energy & Environmental Science* **2013**, *6*, 2338.

(41) Kubota, K.; Komaba, S. *Journal of The Electrochemical Society* **2015**, *162*, A2538–A2550.

(42) Liu, Y.; Fan, F.; Wang, J.; Liu, Y.; Chen, H.; Jungjohann, K. L.; Xu, Y.; Zhu, Y.; Bigio, D.; Zhu, T.; Wang, C. *Nano Letters* **2014**, *14*, 3445–3452.

(43) Hong, S. Y.; Kim, Y.; Park, Y.; Choi, A.; Choi, N.-S.; Lee, K. T. *Energy & Environmental Science* **2013**, *6*, 2067–2081.

(44) Senguttuvan, P.; Rousse, G.; Seznec, V.; Tarascon, J. M.; Palacín, M. R. *Chemistry of Materials* **2011**, *23*, 4109–4111.

(45) Stevens, D. A.; Dahn, J. R. *Journal of The Electrochemical Society* **2000**, *147*, 1271.

(46) Barker, J.; Saidi, M. Y.; Swoyer, J. L. *Electrochemical and Solid-State Letters* **2003**, *6*, A1.

(47) Gover, R.; Bryan, A.; Burns, P.; Barker, J. *Solid State Ionics* **2006**, *177*, 1495–1500.

(48) Ponrouch, A.; Monti, D.; Boschin, A.; Steen, B.; Johansson, P.; Palacín, M. R. *J. Mater. Chem. A* **2015**, *3*, 22–42.

(49) Krachkovskiy, S. A.; Bazak, J. D.; Fraser, S.; Halalay, I. C.; Goward, G. R. *Journal of The Electrochemical Society* **2017**, *164*, A912–A916.

(50) Cresce, A. V.; Russell, S. M.; Borodin, O.; Allen, J. A.; Schroeder, M. A.; Dai, M.; Peng, J.; Gobet, M. P.; Greenbaum, S. G.; Rogers, R. E.; Xu, K. *Phys. Chem. Chem. Phys.* **2017**, *19*, 574–586.

(51) Seo, D. M.; Borodin, O.; Balogh, D.; O'Connell, M.; Ly, Q.; Han, S.-D.; Passerini, S.; Henderson, W. A. *Journal of the Electrochemical Society* **2013**, *160*, A1061–A1070.

(52) Wahlers, J.; Fulfer, K. D.; Harding, D. P.; Kuroda, D. G.; Kumar, R.; Jorn, R. *The Journal of Physical Chemistry C* **2016**, *120*, 17949–17959.

(53) Xu, K.; Lam, Y.; Zhang, S. S.; Jow, T. R.; Curtis, T. B. *Journal of Physical Chemistry C* **2007**, *111*, 7411–7421.

(54) Xu, K. *Journal of The Electrochemical Society* **2007**, *154*, A162.

(55) Nielsen, M. A.; Chung, I. I., *Quantum Computation and Quantum Information*; Cambridge University Press: 2010.

(56) J. M. Thijssen, *Computational Physics*, Second Edi; Cambridge University Press: 2007.

(57) Foresman, J. B.; Firsch, Æ., *Exploring Chemistry with Electronic Structure Methods*, Third Edit; Gaussian Inc: 2015.

(58) Stewart, J. J. P. *Journal of Molecular Modeling* **2013**, *19*, 1–32.

(59) Pople, J. A.; Santry, D. P.; Segal, G. A. *The Journal of Chemical Physics* **1965**, *43*, S129–S135.

(60) Hohenberg, P.; Kohn, W. *Physical Review* **1964**, *136*, B864–B871.

(61) Kohn, W.; Sham, L. J. *Physical Review* **1965**, *140*, A1133–A1138.

(62) Perdew, J. P. *AIP Conference Proceedings* **2001**, *577*, 1–20.

(63) Schlegel, H. B. *Wiley Interdisciplinary Reviews: Computational Molecular Science* **2011**, *1*, 790–809.

(64) Schlegel, H. B. *Adv. Chem. Phys.* **1987**, *67*, 249.

(65) Ochterski, J. W.; Ph, D. *Gaussian Inc Pittsburgh PA* **2000**, *264*, 1–19.

(66) Car, R.; Parrinello, M. *Physical Review Letters* **1985**, *55*, 2471–2474.

(67) Okoshi, M.; Yamada, Y.; Yamada, A.; Nakai, H. *Journal of the Electrochemical Society* **2013**, *160*, A2160–A2165.

(68) Okoshi, M.; Yamada, Y.; Komaba, S.; Yamada, A.; Nakai, H. *Journal of The Electrochemical Society* **2017**, *164*, A54–A60.

(69) Foresman, J. B.; Firsch, Æ., *Exploring Chemistry with Electronic Structure Methods*, Second Edition; Gaussian, Inc: 1996.

(70) Frisch, M. J.; Trucks, G. W.; Schlegel, H. B.; Scuseria, G. E.; Robb, M. A.; Cheeseman, J. R.; Scalmani, G.; Barone, V.; Mennucci, B.; Petersson, G. A.; Nakatsuji, H.; Caricato, M.; Li, X.; Hratchian, H. P.; Izmaylov, A. F.; Bloino, J.; Zheng, G.; Sonnenberg, J. L.; Hada, M.; Ehara, M.; Toyota, K.; Fukuda, R.; Hasegawa, J.; Ishida, M.; Nakajima, T.; Honda, Y.; Kitao, O.; Nakai, H.; Vreven, T.; Montgomery, J. A.; Jr.; Peralta, J. E.; Ogliaro, F.; Bearkpark, M.; Heyd, J. J.; Brothers, E.; Kudin, K. N.; Staroverо, V. N.; Keith, T.; Kobayashi, R.; Normand, J.; Raghavachari, K.; Rendell, A.; Burant, J. C.; Iyengar, S. S.; Tomasi, J.; Cossi, M.; Rega, N.; Millam, J. M.; Klene, M.; Knox, J. E.; Cross, J. B.; Bakken, V.; Adamo, C.; Jaramillo, J.; Gomperts, R.; Stratmann, R. E.; Yazyev, O.; Austin, A. J.; Cammi, R.; Pomelli, C.; Ochterski, J. W.; Martin, R. L.; Morokuma, K.; Zakrzewski, V. G.; Voth, G. A.; Salvador, P.; Dannenberg, J. J.; Dapprich, S.; Daniels, A. D.; Barkas, O.; Foresman, J. B.; Ortiz, J. V.; Cioslowski, J.; Fox, D. J. Guassian 09, Revision B.01, 2010.

(71) Jónsson, E.; Johansson, P. *Physical Chemistry Chemical Physics* **2012**, *14*, 10774.

(72) Chen, S.; Ishii, J.; Horiuchi, S.; Yoshizawa-Fujita, M.; Izgorodina, E. I. *Phys. Chem. Chem. Phys.* **2017**, *19*, 17366–17372.

(73) De, S.; Boda, A.; Ali, S. M. *Journal of Molecular Structure: THEOCHEM* **2010**, *941*, 90–101.

(74) Klamt, A.; Schüürmann, G. *J. Chem. Soc., Perkin Trans. 2* **1993**, 799–805.

(75) Seo, D. M.; Borodin, O.; Han, S.-D.; Boyle, P. D.; Henderson, W. A. *Journal of the Electrochemical Society* **2012**, *159*, A1489–A1500.

(76) Borodin, O.; Suo, L.; Gobet, M.; Ren, X.; Wang, F.; Faraone, A.; Peng, J.; Olguin, M.; Schroeder, M.; Ding, M. S.; Gobrogge, E.; Von Wald Cresce, A.; Munoz, S.; Dura, J. A.; Greenbaum, S.; Wang, C.; Xu, K. *ACS Nano* **2017**, *11*, 10462–10471.

(77) Borodin, O.; Olguin, M.; Ganesh, P.; Kent, P. R.; Allen, J. L.; Henderson, W. A. *Physical Chemistry Chemical Physics* **2016**, *18*, 164–175.

(78) Blint, R. J. *Journal of The Electrochemical Society* **1995**, *142*, 696–702.

(79) Spångberg, D.; Hermansson, K. *Chemical Physics* **2004**, *300*, 165–176.

(80) Kamath, G.; Cutler, R. W.; Deshmukh, S. A.; Shakourian-Fard, M.; Parrish, R.; Huether, J.; Butt, D. P.; Xiong, H.; Sankaranarayanan, S. K. R. S. *The Journal of Physical Chemistry C* **2014**, *118*, 13406–13416.

(81) He, M.; Lau, K. C.; Ren, X.; Xiao, N.; McCulloch, W. D.; Curtiss, L. A.; Wu, Y. *Angewandte Chemie International Edition* **2016**, *55*, 15310–15314.

(82) Okoshi, M.; Chou, C.-P.; Nakai, H. *The Journal of Physical Chemistry B* **2018**, *122*, 2600–2609.